The Impact of a Wet S-Band Radome on Dual-Polarized Phased-Array Radar System Performance

Alessio Mancini, *Student Member, IEEE*, Rodrigo M. Lebrón, *Student Member, IEEE*, and Jorge L. Salazar, *Senior Member, IEEE*

Abstract—This paper discusses the impact of a wet flat radome on the performance of a line replaceable unit active phased-array antenna developed for a dual-polarized phased-array weather radar. Water formations, such as film and droplets, were fully characterized over flat and curved radome surfaces using an analytical model as a function of the precipitation rate. Numerical simulations and experimental results validated the proposed analytical model. An active dual-polarized phased-array of 8 × 2 elements was used to evaluate the degradation of the cross-polarization component as well as the mismatch and the phase of scanned antenna radiation patterns for vertical and horizontal polarizations. In addition, a radome panel of an S-band weather radar (WSR-88D) was characterized in the far field using a single radio-frequency probe. It is demonstrated that even at the S-band, the water formation on the radome affects both copolarization and cross-polarization components, degrading the overall performance of the dual-polarized radar system under rain conditions.

Index Terms—Microstrip arrays, phased arrays, radomes.

I. INTRODUCTION

A RADOME provides electromagnetic transparency and structural strength to protect a radar antenna from the environment. Electromagnetic transparency consists of low reflections, low transmission loss, and minimum distortion of polarization-dependent antenna patterns. The radome also provides structural strength to protect the radar antenna from wind loading and provides stability and integrity for mitigating environmental conditions such as temperature, humidity, and pressure. In addition, the radome facilitates operation and maintenance of the system, increasing its life span [1], [2]. An adverse effect of the radome is the performance degradation of the radio signal when water or ice is present on the outer surface. A radome is designed to minimize the attenuation of the radar signal under dry conditions. This design choice also assures that the attenuation is minimized when a water layer is present on its surface. It is not possible to design a radome for a given rain rate, since the rain

intensity constantly changes, and also because various water formations occur on the radome and generate different attenuations. Depending on the frequency of operation, rain intensity, wind conditions, and its shape and materials, a radome can significantly attenuate, reflect, and depolarize the signal. For frequencies below S-band, the impact of a wet radome is relatively small and cannot be considered critical for radar operations. However, for higher frequencies, water formation on the radome surface can significantly deteriorate the radar signal. The attenuation generated by water accumulated on the radome surface of satellite systems operating between 17 and 22 GHz was extensively analyzed in [3]–[10].

In dual-polarized weather radars, target accuracy is required for polarimetric products such as the differential reflectivity (Z_{DR}) and linear depolarization ratio (LDR) [11], [12]. A mismatch between the horizontal and vertical polarized radiation patterns, as well as a rise of the cross-polarization component, introduces a bias in the measurements of Z_{DR} and LDR. A cause of the mismatch and rise of the cross polarization is the presence of water on the radome. Studies on wet radomes for dual-polarized X-band radars were performed in [13]–[15]. Different water formations on the radome surface were analyzed by Salazar-Cerreño *et al.* [16]. Díaz *et al.* [17] evaluated the effect of the radome, both under dry and wet conditions, as a function of the tilting angle. Mancini *et al.* [18]–[20] proposed a real-time measurement instrument to account for losses occurring on the wet radome while the radar is scanning. Studies to evaluate the attenuation of wet radomes at C-band were performed by Frech *et al.* [21] and Kurri and Huuskonen [22]. Despite the numerous publications available for wet radome characterization at frequencies higher than the C-band, the literature about the S-band is limited. Some quantitative analysis is presented in [23]–[27]. Effenberg *et al.* [24] measured up to 3 dB attenuation when water distributes as a film at 50 mm h^{-1} rain rate. Merceret and Ward [26] empirically found that at the rain rate of 200 mm h^{-1}, the two-way attenuation is 5.6 dB for film formation and 1.95 dB when water accumulates as droplets.

In this paper, a new research method to quantify the impact of a wet flat radome on the antenna radiation pattern operating at the S-band is presented. The study aims to investigate the impact of different water formations located in the near-field

region of an antenna protected by a flat radome. The novel aspect of the method presented in this paper consists of using a near-field chamber to characterize the effects of water on the radiation pattern of the antenna under test. The water formations considered are film, droplets, and rivulets. In Section II, an analytical model was created to compute the film thickness and droplet residual that accumulates on a squared flat radome at various combinations of tilting angles and rain rates. Then, by using the Maxwell–Garnett equation, the equivalent dielectric constant of the layer composed of droplets enclosed in an air volume was computed. Finally, by performing numerical simulations, the reflectance and transmittance through a multilayer radome, including the water layer, were calculated. Scattered field generated from the droplets might also contribute to attenuation, but to account for it would overcomplicate the numerical analysis, as will be discussed later in this paper. Two types of experiments performed on wet S-band radomes will be discussed in Section IV. The first tests consisted of characterizing a radome sample in far field using a single radio frequency (RF) probe [18]–[20]. To measure the effect of water on the far-field radiation pattern, a novel experiment was performed in a near-field chamber on an 8×2 dual-polarized phased array antenna [28]. These tests were executed to evaluate the amplitude and phase degradation of the far-field radiation pattern of the antenna, when water was present in the near-field region of the antenna. A good match was achieved between the measured and computed attenuation, validating the proposed approach.

II. ANALYTICAL MODEL FOR WET RADOME CHARACTERIZATION

Depending on the hydrophobic property of the radome outer skin, water distributes either as droplets and rivulets, or as a continuous film. The first scenario occurs in cases when the radome outer skin is covered with a hydrophobic coating, while the second case happens when the raincoat is not water-repellent (hydrophilic). Examples of different water formations are presented in Fig. 1. An analytical model to characterize various water formations (continuous film or droplets) was developed to estimate the amount of water accumulated on a squared radome surface inclined at different angles under various rain rates. First, the laminar flow formation will be shown, which corresponds to a surface with hydrophilic characteristics. Then, the droplet case will be presented, corresponding to the scenario of a hydrophobic radome.

A. Continuous Film

Water distributes as a continuous film rather than droplets when the raincoat does not have hydrophobic characteristics anymore. The film might not be uniform in real scenarios, due to radome imperfections or wind presence. In this paper, a uniform laminar flow is assumed for the purpose of not overcomplicating the model. The thickness of the water film accumulated on a flat surface can be computed as a function of the rain rate and tilting angle as in [29]

$$t_{film} = \sqrt[3]{\frac{3\Gamma\mu}{\rho^2 g \sin\theta_i}} \qquad (1)$$
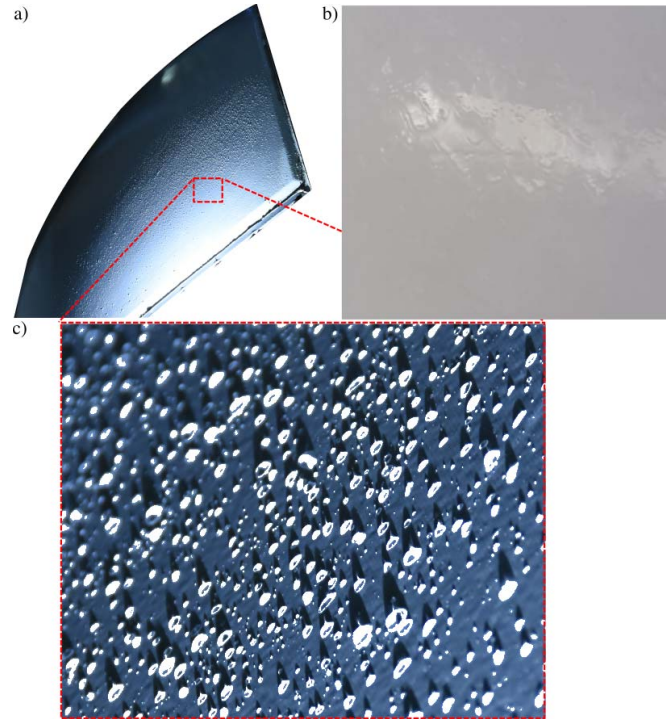
Fig. 1. Droplets and film formations occurring on the radome. (a) Panel of the WSR-88D radome. (b) Closeup of the radome showing water distributed as a continuous film. (c) Closeup of the radome panel showing the droplet formation.

where μ is the dynamic viscosity of water (10^{-3} kg m^{-1} s^{-1}), ρ is the density of water (998.2 kg m^{-3}), g is the gravitational acceleration (9.81 m s^{-2}), θ_i is the inclination angle with respect to the horizontal plane, and Γ is the liquid mass flow rate per unit width of surface (kg m^{-1} s^{-1}). The relationship between Γ and the rain rate (R) for a square flat radome is given as

$$\Gamma = \rho \frac{R A_p}{3600 \times 10^3} \frac{1}{W}. \qquad (2)$$

The denominator in (2) expresses the rainfall rate in m s^{-1}. Furthermore, because the rain rate is defined as the water accumulated per unit time on a surface of 1 m^2, it is necessary to scale the rain rate to the area of the radome projected in the direction of the rain (A_p, where subscript p stands for "projected"). Finally, W is the width (m) of the radome. The projected area for a square radome, computed in the direction of fall of the rain, is given as

$$A_p = W^2 \cos\theta_i. \qquad (3)$$

The film thickness computed as a function of the rain rate, at various inclination angles of the surface, is shown in Fig. 2.

B. Droplets

The drop-size distribution (DSD), indicated with $N(D)$, is the parameter commonly employed to describe the amount of droplets of a specified diameter contained in 1 m^3 volume of
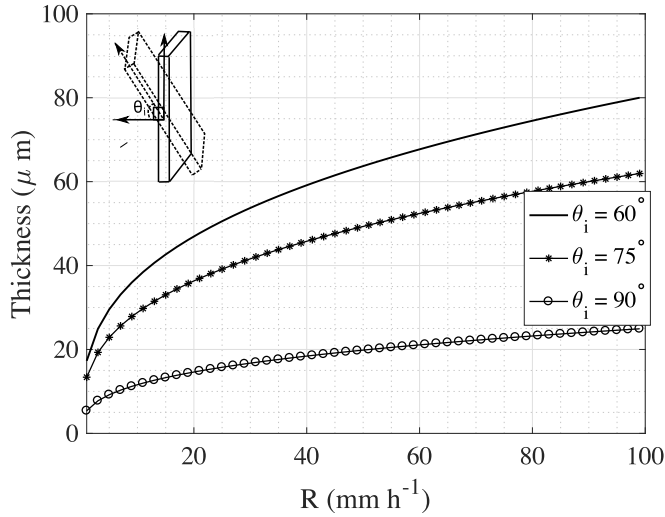
Fig. 2. Film thickness calculated as a function of the rain rate, at different inclination angles (with respect to the horizontal plane) of the radome surface.

air. The gamma distribution was used to estimate the DSD [30]

$$N(D) = N_0 D^u \exp(-\Lambda D)$$
$$\Lambda = 4.1 R^{-0.21}$$
$$N_0 = 8 \cdot 10^3$$
$$u = -0.016\Lambda^2 + 1.213\Lambda - 1.957 \qquad (4)$$

where $N(D)$ units is $m^{-3} \, mm^{-1}$, D represents the drop diameter (mm), and R is the rain rate (mm h^{-1}). The DSD at different rain rates is plotted in Fig. 3(a). To account for the droplet accumulation on a flat radome with unit surface area A_u (m^2), it is necessary to first compute the terminal velocity (m s^{-1}) of the droplets [31] and [32] as

$$v(D) = 386.6 D^{0.67} \qquad (5)$$

where D is the droplet diameter (m). The droplet residual, or the total number of droplets accumulated per diameter class on a surface A_u (m^2) that is inclined at an angle θ_i with respect to the horizontal, computed for an observation time T (s), is given as [33]

$$n_R(D) = N(D) A_u v(D) T \Delta D \cos \theta_i \qquad (6)$$

where ΔD is the diameter interval (mm). The $\cos \theta_i$ term is used to calculate the projection of A_u in the direction of the fall of the droplets at the inclination angle θ_i. The droplet residual on an area of dimensions equal to $\lambda \times \lambda$ ($\lambda = 10.53$ cm at 2.85 GHz), for $T = 30$ s and $\Delta D = 0.5$ mm, is plotted in Fig. 3(b) and (c) for $\theta_i = 89°$ and $75°$, respectively. It was not possible to generate the plot that corresponds exactly to 90° of inclination, because the cosine in (3) becomes zero. Therefore, instead of 90°, 89° was chosen as a good approximation to evaluate $n_R(D)$. The breakup that occurs as a consequence of the droplet impacting the radome surface was not taken into account because it was too complicated to model.

In cases when the droplet removal from the radome surface is known, and the rain rate must be found, the DSD can be calculated by inverting (6). Then, the rain rate is obtained by [32]

$$R = \frac{6\pi}{10000} \sum_{D_{min}}^{D_{max}} N(D) v(D) D^3 \Delta D. \qquad (7)$$

The reason for introducing (7) will be clarified later in Section IV.

To create a more accurate model, it is necessary to account for raindrops that fall off the radome surface at a specific inclination angle. Droplet removal occurs when the component of the gravity force parallel to the inclination plane defeats the surface tension at the water–radome interface. Therefore, droplets with larger diameter will fall off the surface. The tilting angle at which a droplet with a given diameter starts moving is called the critical angle (θ_{crit}). The critical angle, which depends on the hydrophobic property of the surface, is evaluated by [34]

$$\theta_{crit} = \text{asin} \frac{(k^{-1})^2 \sin(\pi - \theta)(cos\theta_R - cos\theta_A)}{4/3\pi r^2} \qquad (8)$$

where k^{-1} is the capillary length of water (2.7 mm), θ_A and θ_R are the advancing and receding angles, $\theta = (\theta_A + \theta_R)/2$, and r is the radius of the droplet. θ_A and θ_R depend on the hydrophobicity of the raincoat of the radome. The smaller the difference between θ_A and θ_R (hysteresis angle), the more hydrophobic is the surface. From (8), it is immediately obvious that the bigger the droplet, the smaller is the angle of inclination required to make the droplet fall. A comparison of critical angles for different materials is shown in Fig. 3(d).

To complete the analytical model, the final step is to estimate the attenuation due to droplet residual (n_R) accumulated on the square radome. To account for this, a simulation was developed to randomly place these residual droplets on a lattice that represents the radome surface of dimensions $\lambda \times \lambda$ (where $\lambda = 10.53$ cm). The lattice resolution was 0.05 mm. Since two droplets could be placed to overlap each other, and because it is necessary to account for the droplet removal at a specific critical angle, the simulation replaces two droplets that intersect with one equivalent droplet. The equivalent droplet has a volume that is the sum of the volumes of the two overlapping droplets. The diameter of the equivalent droplet is computed from the equivalent volume. Then, if the corresponding diameter is too large [Fig. 3(d)], the droplet is removed. The process is repeated until all droplets accumulated (6) are placed on the lattice. An example of operation of this simulation for $R = 10$ mm h^{-1}, $\theta_i = 75°$, considering Teflon as a raincoat [Fig. 3(d)], is shown in Fig. 4 for the observation times of 1–9 mins. In Fig. 4(a), DSD and n_R were calculated choosing $\Delta D = 0.1$ mm, only for the purpose of generating smoother curves, while in the following simulations [Fig. 4(b)–(d)], ΔD was selected to be equal to 0.5 mm instead of 0.1 mm, to limit the simulation time.

To estimate the attenuation due to the layer of droplets on the radome, it is necessary to first compute the effective dielectric constant (ϵ_{eff}) by using Maxwell–Garnett's equation [35]

$$\epsilon_{eff} = \epsilon_e + \frac{3\delta_i \epsilon_e (\epsilon_i - \epsilon_e)}{\epsilon_i + 2\epsilon_e - \delta_i(\epsilon_i - \epsilon_e)} \qquad (9)$$
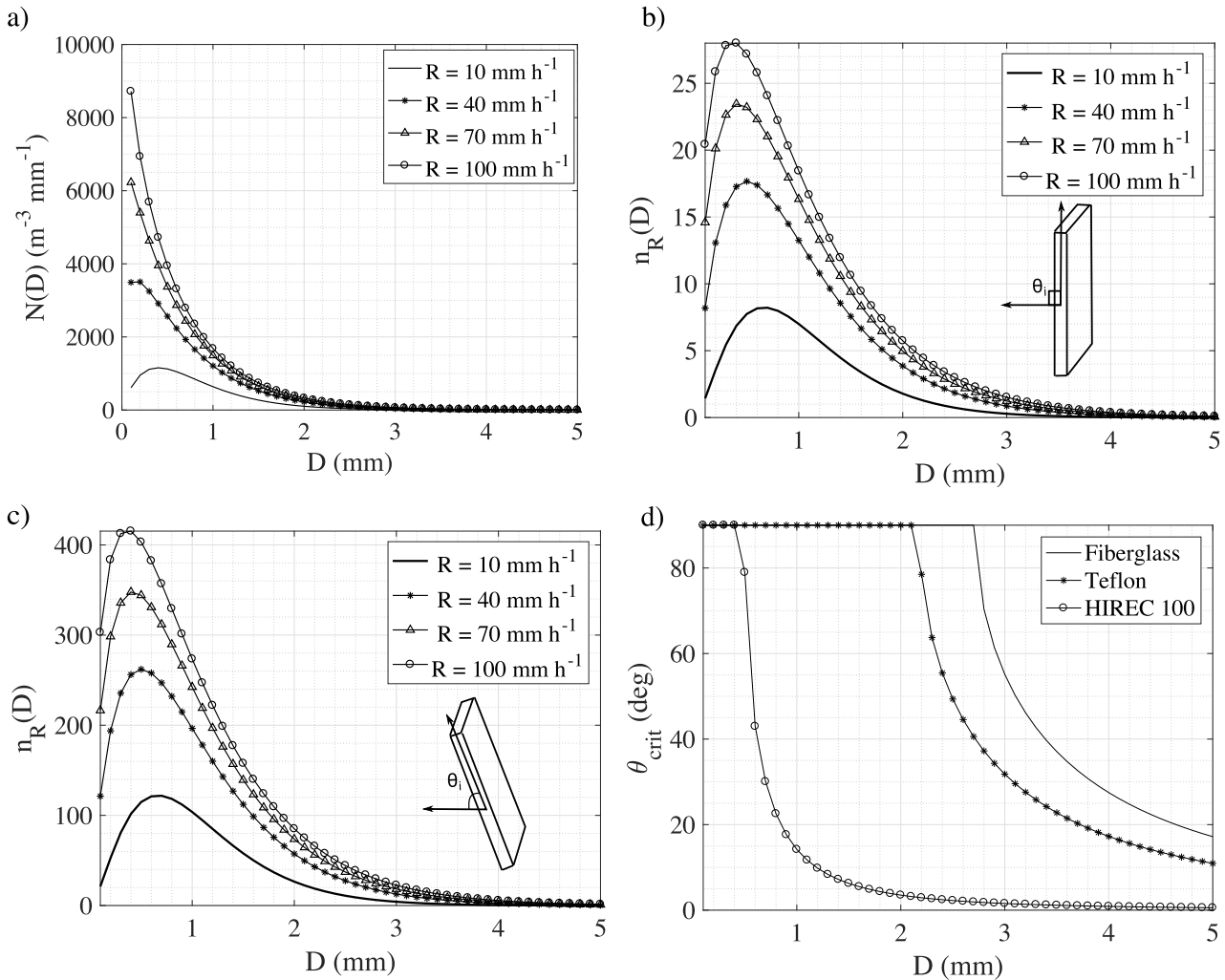
Fig. 3. (a) DSD, $N(D)$, computed at different rain rates. (b) and (c) Number of droplets accumulated, $n_R(D)$, on a 10.53×10.53 cm^2-surface for $T = 30$ s, evaluated for different rain rates, at $\theta_i = 89°$ and $75°$, respectively. (d) Computed critical angles, θ_{crit}, for fiberglass (hydrophilic), Teflon (hydrophobic), and HIREC 100 (superhydrophobic). The advancing and receding angles are $105°$ and $15°$ for fiberglass, $120°$ and $79°$ for Teflon, and $151°$ and $144°$ for HIREC 100.

where ϵ_e is the dielectric constant of the enclosure (air) and ϵ_i is the dielectric constant of the enclosed spheres (water). δ_i is the fractional volume calculated as the ratio between the total volume of water and the rectangular air volume that encloses the droplets. In conclusion, a numerical simulation was performed to compute the reflectance and transmittance of the layer of droplets with dielectric constant ϵ_{eff}. The reason for modeling the layer of droplets with an equivalent material of laminar shape with dielectric constant ϵ_{eff} is to reduce the simulation time, without affecting the accuracy of the results.

III. NUMERICAL ANALYSIS

In this section, numerical results performed with high-frequency structure simulator (HFSS 2017) software will be shown and discussed. The analysis was conducted using the infinite array approach. The infinite array approach involves replicating a radome unit cell to the infinite along x and y coordinates [Fig. 5(d)]. The stackup of the sandwich radome is listed in Table I. The numerical study consisted of evaluating

TABLE I
WSR-88D RADOME STACKUP EMPLOYED IN THE NUMERICAL SIMULATIONS TO ESTIMATE THE ATTENUATION. THE RADOME IS DESIGNED TO OPERATE AT 2.85 GHz

Material	Thickness (mm)	ϵ_r	tanδ
Raincoat	0.28	3.75	0.06
Fiber-glass (outer skin)	1.3	4.2	0.012
Foam (core)	24.73	1.09	0.0017
Fiber-glass (inner skin)	1.3	4.2	0.012

the reflectance and transmittance introduced by a wet radome. Different rain intensities for various inclination angles were calculated based on the formulations provided in Section II. In general, numerical simulations are accurate because they are able to account for absorption occurring in the water layer. Film formation on a multilayer radome can be easily modeled numerically because the rectangular shapes of the composing materials do not require a dense mesh. For droplet formation on the radome, a numerical study can account for the small
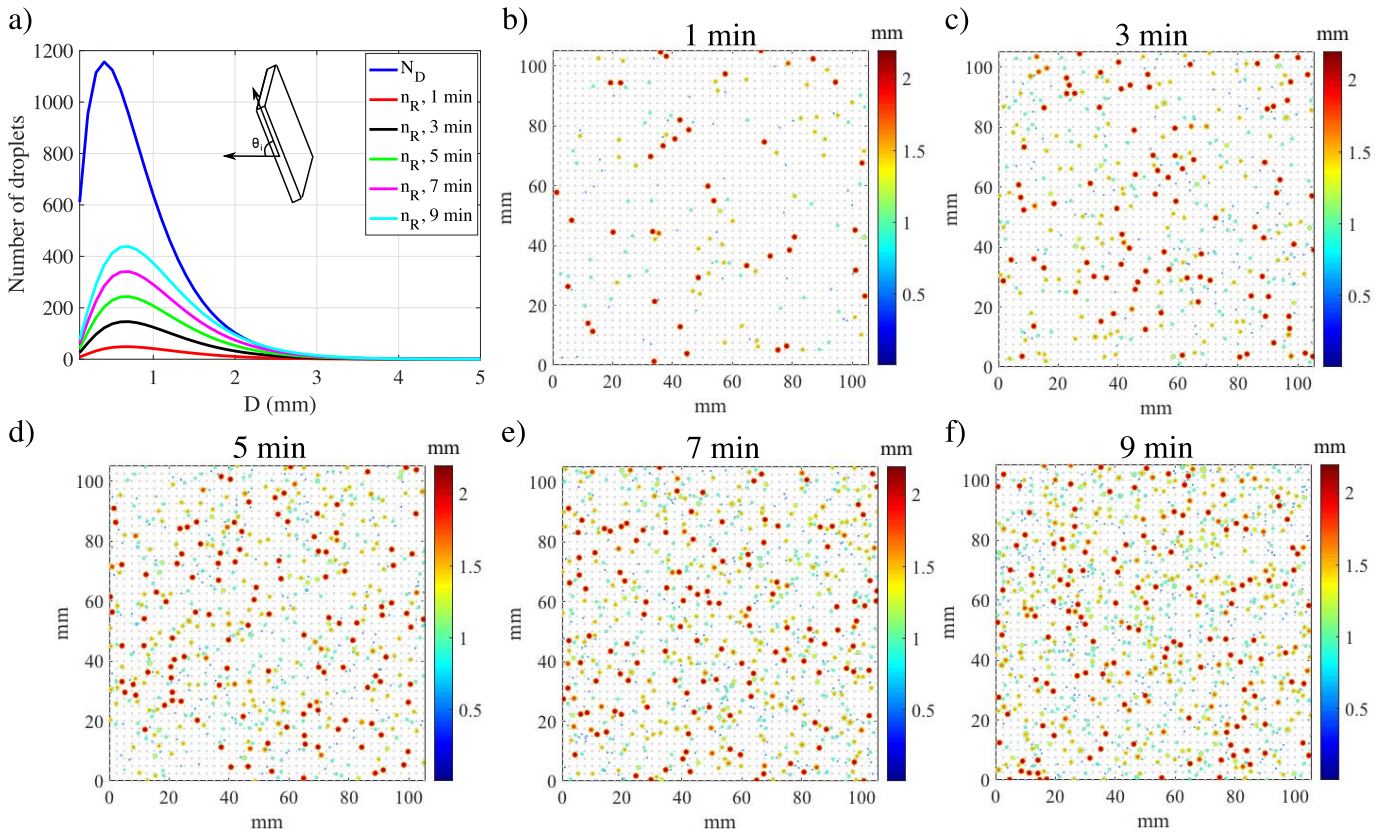
Fig. 4. Example runs of the simulation in MATLAB of raindrop accumulation on a flat radome panel, for $R = 10$ mm h^{-1}, $\theta_i = 75°$, and $\Delta D = 0.5$ mm. The raincoat chosen was Teflon. (a) DSD compared to the droplet residuals computed for $T = 1$–9 mins with a step of 2 min. (b)–(f) Droplet residuals on the lattice, after having accounted for the droplet agglomeration and removal for 1–9 mins, respectively. Color bar: droplet diameters.

amount of absorption occurring inside the droplets and also for the scattering generated by the spherical geometry of the droplets. However, modeling spheres of small dimensions requires a very dense mesh, increasing simulation time and computational memory. To decrease the computational effort, the layer of droplets was modeled as a rectangular slab with the dielectric constant computed by the Maxwell–Garnett equation. This choice does not account for scattering generated by the spheres but neglecting scattering does not introduce a significant error.

The radome stackup and the related electromagnetic parameters are listed in Table I. The dimensions of the radome unit cell are $\lambda \times \lambda$ ($\lambda = 10.53$ cm).

A. Continuous Film

The dielectric constant and tangent loss of water at 2.85 GHz are 78.2 and 0.1579. The thicknesses of the water film were computed by using (1) and are plotted in Fig. 2. Only results corresponding $\theta_i = 75°$ are presented for the sake of brevity. Results of numerical simulations are presented in Fig. 5 as a function of the steering angle in elevation (θ_s), for both H- and V-planes. The reflectance is plotted in Fig. 5(a). It is noticed that the level of reflection rises noticeably as a layer of water is added to the dry radome. This results in an increase of the sidelobe level (SLL) of the radar antenna. Furthermore, for beams steered at angles higher than 20°,

the reflectance is higher for the H-polarization than for the V-polarization. Similar conclusions can be drawn for the transmittance [Fig. 5(b)]. For a dry radome, the attenuation starts from a minimum of 0.06 dB at the broadside and reaches a maximum of 0.6 dB at 60° of steering angle for H-polarization. When the radome is wet, at the broadside, the attenuation starts from a minimum of 0.2 dB and reaches a maximum of 0.4 dB. Losses increase as the steering angle rises for the H-polarization. For the V-polarization, the minimum attenuation is reached at 75°. In Fig. 5(c), the phase of the transmittance is shown. The thicker the water layer is, the higher is the phase shift. A phase shift of 6° occurs for the thinnest layer of water, and one of 11° manifests for the thickest film. The H-polarization presents a larger change in the phase than the V-polarization. In Fig. 5(d), a schematic representation of the unit cell of the infinite array approach is presented. In this figure, also indicated are the master and slave boundary conditions (M- and SL-BC).

B. Droplets

In Section II, n_R was introduced (6). Then, by considering Teflon as the outer layer of the radome, at a specific inclination angle, the amount of droplets that remained on the surface was computed (8). The remaining droplets were placed on a square lattice as shown in Fig. 4. In this paragraph, droplet placements obtained for each observation time shown for
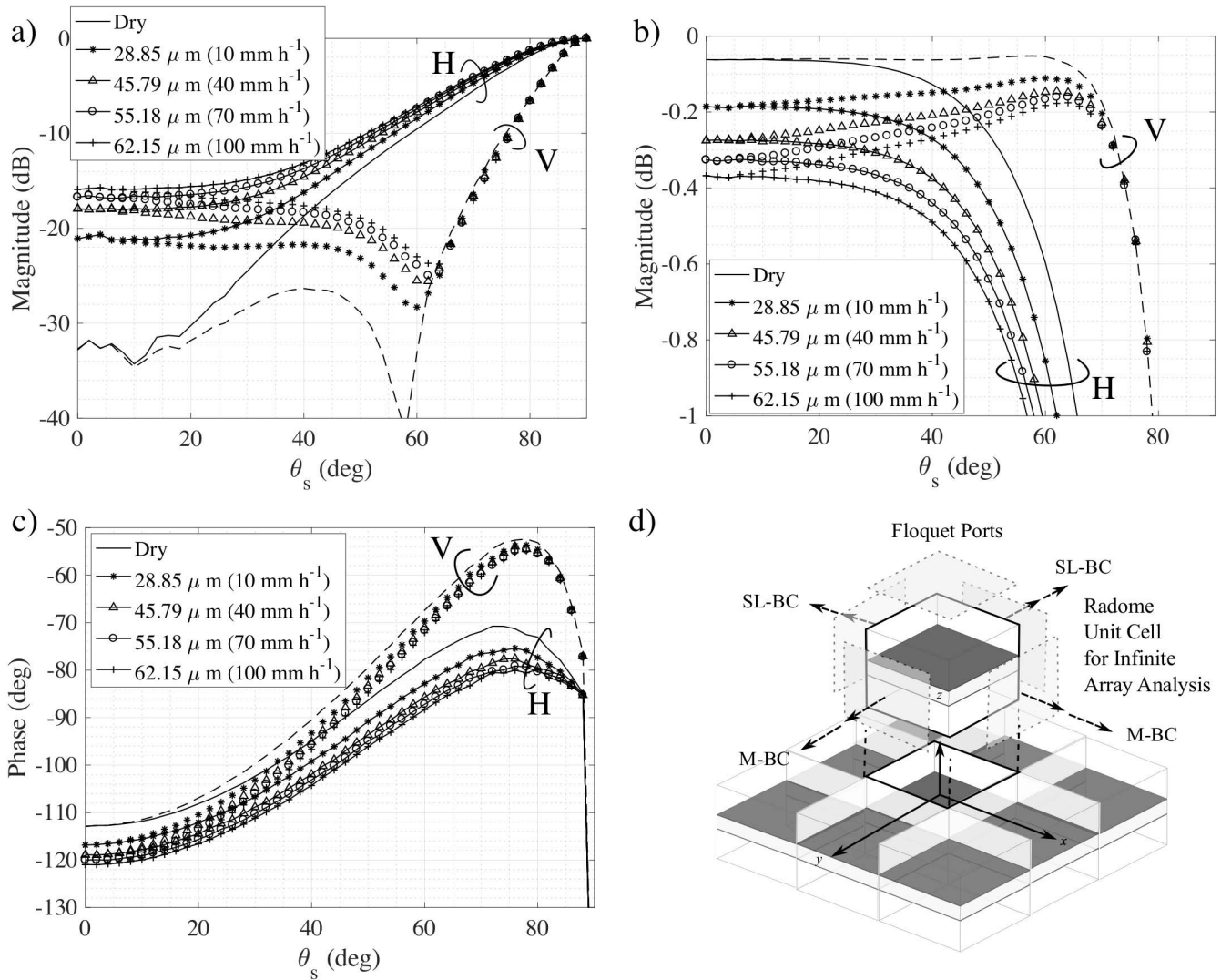
Fig. 5. Numerical simulations performed for different film thicknesses, for H- and V-polarizations (continuous and broken lines, respectively), at the inclination angle of 75°. (a) Reflectance. (b) Transmittance. (c) Phase of the transmittance. (d) Schematic representation of the infinite array approach showing the unit cell and its replication along the x- and y-axes.

$R = 10$ mm h^{-1} [Fig. 4(b)–(f)] are validated numerically. The droplet accumulation, corresponding to each observation time considered, was modeled by using an equivalent layer with a dielectric constant computed by (9). The infinite array approach used for the film formation is also employed for this case. The unit cell was 10.53×10.53 cm^2, as it was for analyzing the film formation. Results are presented in Fig. 6(a) for the reflectance as a function of the frequency. As apparent, by increasing the observation time, reflectance increases at the resonant frequency. In Fig. 6(b), the transmittance is plotted versus frequency. The highest attenuation occurs for 9 min observation time and is only 0.065 dB at 2.85 GHz. This value lies within Merceret's loss range [26], providing additional validation for the chosen approach. The reflectance and transmittance as a function of the steering angle are shown in Fig. 6(c) and (d). Also, as expected, for the droplet formation, attenuation increases with the steering angle, although at smaller magnitude than in the case of the film.

IV. EXPERIMENTS

RF characterization of a wet radome was performed using two types of experiments. The first one, described in [18], employs a single probe to measure the attenuation introduced in the far field by a radome panel of an operative weather radar (WSR-88D) and provides validation for the second method (Section IV-B). The second type of experiment is a new approach developed at the Advanced Radar Research Center. The novelty of this experiment is that the radome is characterized in a near-field anechoic chamber by measuring the radiation pattern of the antenna under test in the presence of water. Tests performed with the new technique employed an 8×2 phased array radar (PAR) antenna.

A. Far-Field Radome Characterization

The performance of a radome panel of the WSR-88D radar (2.7–3 GHz) was tested under both dry and wet conditions at orthogonal incidence. The radome panel is of pentagonal shape
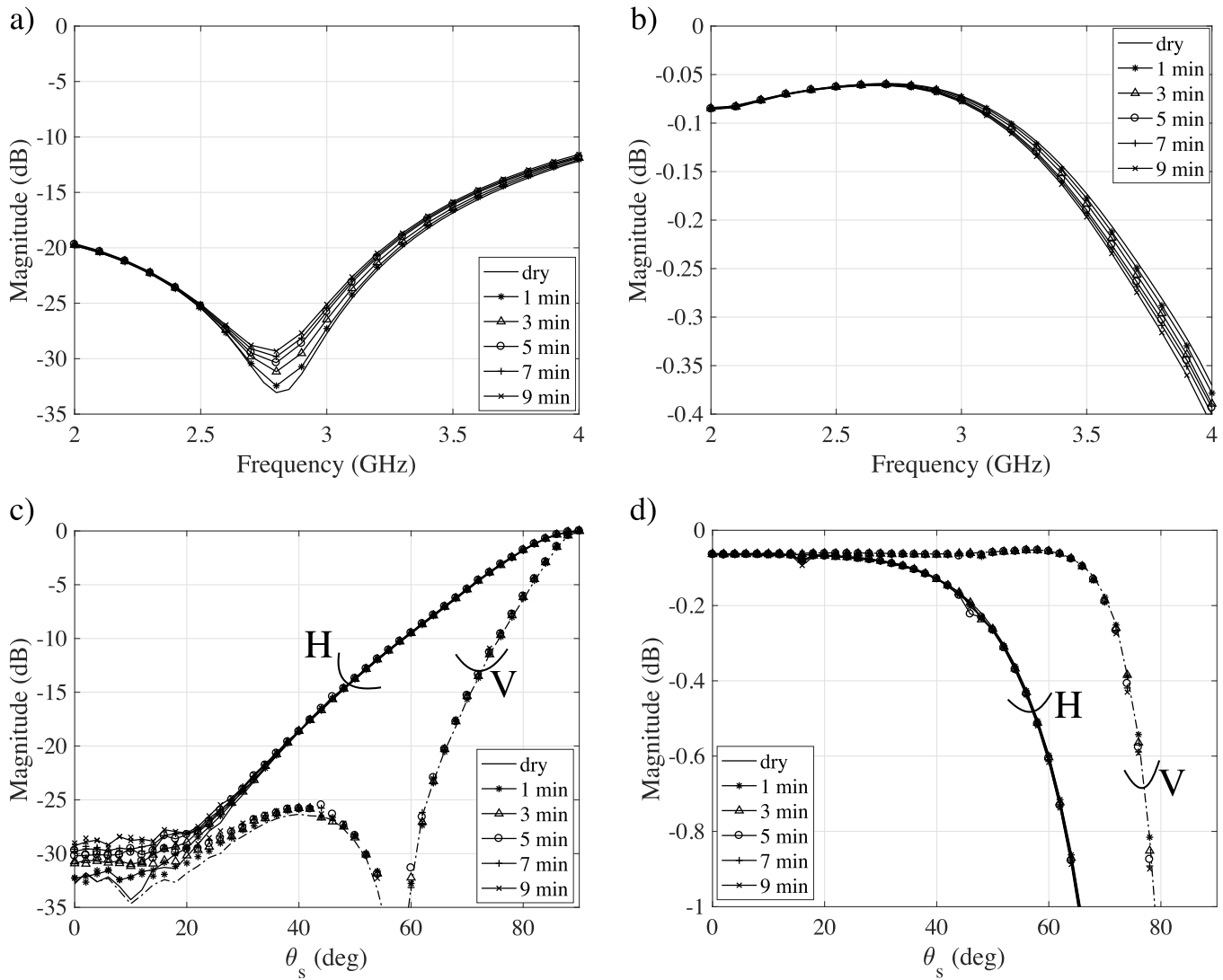
Fig. 6.   Numerical simulations performed for the droplet scenarios shown in Fig. 4. The droplet layer was modeled by using the Maxwell–Garnett equation. Results are presented for H- and V-polarizations. The frequency responses of the (a) reflectance and (b) transmittance at normal incidence. (c) Reflectance and (d) transmittance calculated at various steering angles, at 2.85 GHz.

and is shown in Fig. 7(a). The dimensions of the panel are 2.34 m in height and 2.27 m in width. The method employed for RF characterization used a single probe connected to a reflectometer to measure the folded reflectance generated from the multilayer radome. By using the time-domain gating (TDG) analysis, implemented in the reflectometer, it is possible to minimize the effect of multiple reflections coming from the surrounding environment, and therefore improve the data quality. The single-probe method, as well as the benefit of employing TDG, was discussed in [18] and [19]. In this research, a horn antenna (2.6–3.95 GHz) was used to characterize the RF performance of the WSR-88D radome. The reflectometer employed is the R140 series by Copper Mountain, which operates in the range from 85 MHz to 14 GHz with a pulse repetition frequency of 30 KHz. Further technical aspects of this device are discussed in [18]. To have good spatial resolution in the time domain, the frequency range should be as wide as possible. The largest possible band of

operation of the reflectometer is dictated by the frequency band of the horn antenna, which ranges from 2.6 to 3.95 GHz. The distance from the probe to the radome panel was about 1.5 m, which assured that the horn antenna would operate in the far field. That distance also allowed confining the beam of the horn antenna inside the radome sample (no fringing effect from the borders). The start and stop times of the gating function were 6.8 and 7.28 ns. The probe was mounted on a robotic arm to assure good stability and accuracy during the measurements. The robotic arm also allowed keeping the horn antenna aligned with the center of the radome when the probe was rotated to 90° to measure in the other polarization. The experimental setup is shown in Figs. 7(a) and 8(d).

Radome performance was initially measured under dry conditions for both polarizations. Then, a subsequent experiment repeated the first but used an ordinary sprinkler to wet the radome. The sprinkler was placed on a pole in front of the radome panel, outside of the range of time gating, to make
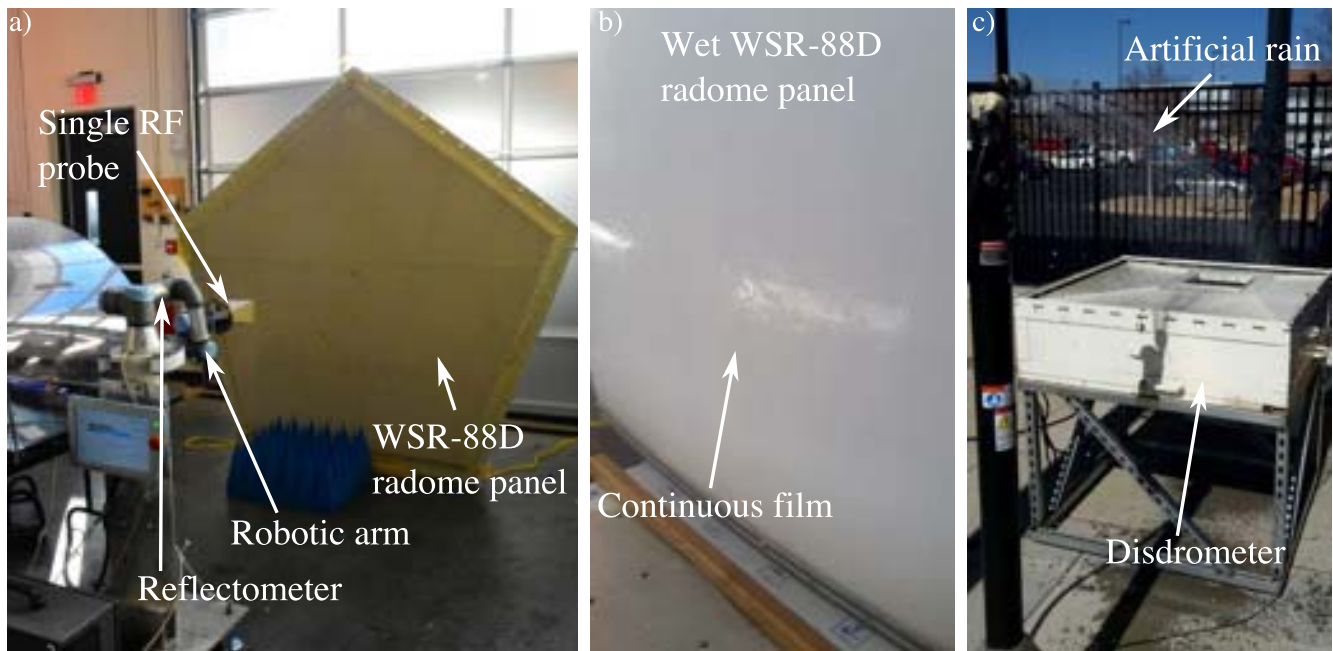
Fig. 7.   Experimental setup employed to characterize the RF performance of the WSR-88D radome panel in the far field. (a) Radome panel, probe, and reflectometer mounted on the robot arm. (b) Photograph taken during the experiment under artificial rain conditions, showing the water distributing as a continuous film. (c) 2-DVD employed to measure the rain rate of the sprinkler.

sure that the reflections produced by the pole were filtered. The sprinkler wet the radome at the top, and water flowed naturally down to the base of the radome. Since the radome panel was not new, the hydrophobic property of the raincoat had been exhausted before the experiments were conducted. Therefore, water is distributed as a film, as shown in Fig. 7(b). To have an approximate measurement of the rainfall rate produced by the sprinkler, a 2-D video disdrometer (2-DVD) was used. The sprinkler mounted on the pole and the 2-DVD are presented in Fig. 7(c). The measured rain rate was not constant because wind moved the water beam away from the aperture of the disdrometer, causing only a portion of the water to fall inside the sampling window. The measured rain rate is shown in Fig. 8(a). The average and peak rain rates are 63 and 102 mm h^{-1}. The measured reflectance for the dry, wet, and drying scenarios is shown in Fig. 8(b). The curves plotted in the time domain are obtained as an average of the reflectance measured in the frequency domain over all of the bandwidth selected (2.6–3.95 GHz). These curves are normalized with respect to the reflectance obtained by placing a metal plate behind the radome for the purpose of calibration. As expected, the curve corresponding to the dry scenario presents the lowest reflectance, while the one obtained under wet condition produces the highest values of reflectance. The curve that represents the drying case was measured when water was no longer sprayed on the radome. Therefore, the amount of water on the radome was lower than in the wet scenario. Since these tests were performed using a single probe, it was not possible to directly measure the transmittance, because absorption (A) occurs ($T = 1 - R - A$). However, it was demonstrated in [18] and [19] that by knowing the rain rate, it is possible to compute the thickness of the water film accumulated on the

radome. By executing a numerical simulation, it was possible to estimate the attenuation of the signal crossing the water layer. Therefore, the transmittance can be indirectly computed. For the simulation, the thickness of the water layer was computed by using Gibble's formula [3], also employed in [18]. To compute the thickness of the water film, the highest rain rate registered during the experiment [102 mm h^{-1}, Fig. 8(a)] was used. The radius of the spherical radome (WSR-88D) was 11.89 m. The calculated thickness was 372 μm. The simulated (continuous line) and estimated (broken line) transmittances are plotted in Fig. 8(c). This figure shows that the estimated transmittance (continuous line) closely approximates the one obtained through numerical analysis, proving the validity of the proposed approach. The transmittance of the drying scenario was not estimated, because it was not possible to evaluate the thickness of the film while the water was drying. In Fig. 8(d), a schematic representation of the technique is presented.

B. Near-Field Radome Characterization

Although radome characterization is commonly performed in the far field, in practical situations, water is located on the outer surface of the radome, which is in the near-field region of the radar antenna. Therefore, to more realistically evaluate the antenna performance with water accumulated on the radome, a different approach was chosen. The method consists of measuring the radiation pattern of a 8×2 linear replaceable unit (LRU) antenna array in a near-field anechoic chamber. With this method, it was possible to characterize the impact of water located in the near-field region of the antenna, on the far-field radiation pattern. The importance of
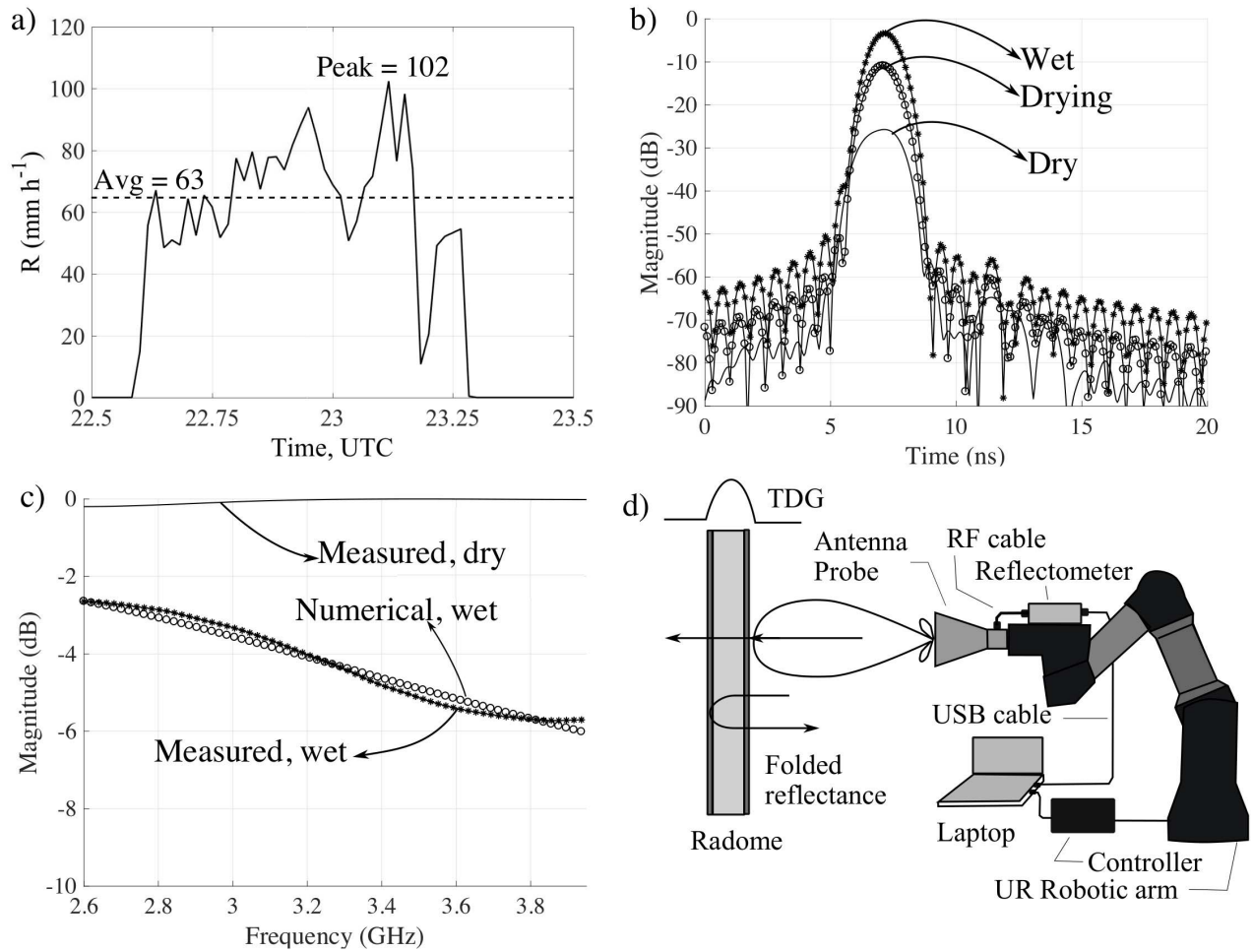
Fig. 8. RF characterization of the WSR-88D radome panel in the far field using the single probe technique. (a) Rain rate generated by the sprinkler and measured from the 2-DVD. (b) Reflectance in the time domain. (c) Transmittances obtained for the dry and wet scenarios compared to the one simulated numerically. (d) Schematic representation of the setup employed for the experiment.

this approach is that it replicates scenarios of water formations on the radome and accounts for the effect of water on the antenna radiation pattern. This would allow a preliminary study to estimate the effect of water on important parameters such as beamwidth, cross polarization, and sidelobe level, before the antenna becomes operative. The antenna array employed for this experiment was a prototype of a dual-polarized 8×8 *S*-band radar antenna array [28], with only the 8×2 subarray being fed. A photograph of the near-field setup, including the active array, is shown in Fig. 9. It is important to clarify that the radome used in this experiment corresponds to the internal radome, that in a PAR is always attached to the antenna surface. In cases where an external radome is employed, results from Section IV-A can be used to evaluate the antenna performance.

Tests were performed both under dry and wet conditions, for H- and V-polarizations, at the steering angles of $-30°$, $0°$, and $30°$. For the wet cases, different scenarios were considered. These scenarios included randomly distributed droplets, vertically aligned droplets, rivulets, and a partial film. To keep water in a steady position during the whole

near-field measurement, an ordinary bubble plastic packing material was used. This solution allowed placing water in the various areas of the active subarray without having the measurements affected by the plastic support. To prove that the bubble plastic (without water) does not introduce any bias in the near-field tests, a comparison of the radiation patterns measured with and without the plastic is presented in Fig. 10. This figure shows that the plastic does not introduce any effect on the far-field radiation patterns of copolarization and cross polarization. Therefore, in the experiments presented later, all changes in the radiation pattern performance must be attributed to the presence of water.

The first experiment measured the near-field radiation pattern of the active array antenna under dry conditions. The subsequent experiments included the presence of water. To record the exact location of water, photographs of the setup were taken with an infrared camera. These are shown in Fig. 11. The reason for employing an infrared camera is not to determine the temperature of the water, which is irrelevant for this experiment but is to highlight the areas of the 8×2 array that were covered with water. Otherwise, the water is not visible
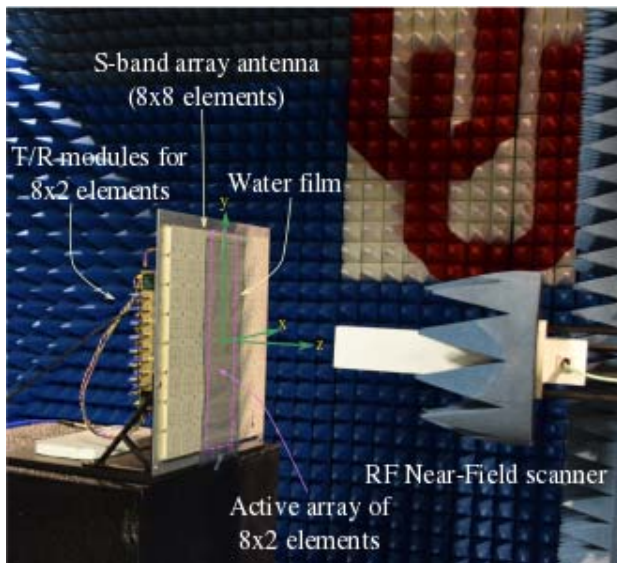
Fig. 9. Photograph of the 8×8 LRU antenna array employed for the near-field measurements, with the water film placed on the radome. In the figure, the active array composed of 8×2 elements is also highlighted.

because it is transparent. The locations occupied by water were made apparent by the slight difference in temperature (2°–3 °C) between the environment and fresh water.

In the second test, water was sprayed on a plastic sheet that overlapped the 8×2 array. Bubble plastic packing material was not used for this test because droplets with an unrealistic diameter would have been produced. By spraying water with a thin nozzle, smaller droplets with various diameters were created. This procedure allowed replication of droplets with diameters similar to what would occur in a real situation. The water distribution obtained for this scenario is shown in Fig. 11(a)–(e). By using a numerical code for imaging recognition, from a photograph of the water distribution, it was possible to estimate the droplets' diameters by postprocessing. Then, by knowing the diameters, the droplet residual (n_R) was computed by using (7). Finally, by choosing $T = 30$ s and $\Delta D = 0.2$ mm, a rain rate of 8.9 mm h^{-1} was calculated. To remain consistent with the physical meaning of θ_i (angle of projection of the radome in the direction of the rain), water was sprayed keeping the nozzle directly pointed at the front of the array. Therefore, the angle was set equal to 0° in (6). The third experiment considered droplets vertically aligned to reproduce rivulets, as shown in Fig. 11(b)–(f).

Because the packing plastic presents bubbles with spaces between them, while rivulets have a continuous geometry, the rivulets were created in a different way in the fourth experiment. To have continuous rivulets, two sheets of plastic were laminated together by using a heat gun. Then, by cutting the sheet in strips, rivulets were obtained. The strips were filled with water. Rivulets of different lengths were made, as shown in Fig. 11(c)–(g). The widths and thicknesses of the continuous rivulets were about 6 and 1.07 mm. Unfortunately, there is no formula that allows relating the rivulet dimensions to an estimation of the rain rate. However, this test still has particular importance because it allows the evaluation of
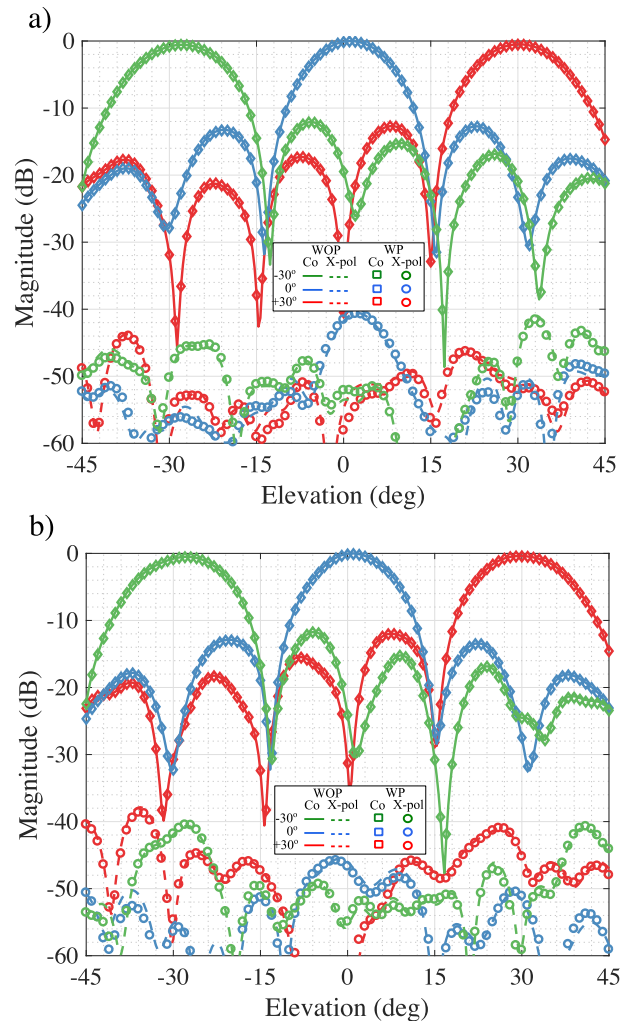
Fig. 10. Comparison of the measured radiation patterns of the 8×2 array, at the steering angles of $-30°$, $0°$, and $30°$, without plastic (WOP) and with plastic (WP). (a) H-polarization. (b) V-polarization.

different effects that vertically distributed water have in the H- and V-polarizations. The fifth case examined was film formation. Since a film is hard to replicate, an approximate and practical solution was obtained by layering two sheets of plastic to obtain a rectangular pocket of area equal to the area of the 8×2 array. To assure uniform water distribution across the whole 8×2 array, cells were created inside the pocket. These cells allowed the distribution of water all over the area equivalent to the subarray, leaving only a few portions uncovered. Photographs taken of the water film are shown in Fig. 11(d)–(h). Physical limitations of the setup employed to produce the film formation caused a lack of uniformity in the film thickness and also did not completely fill the area of the 8×2 array [Fig. 11(h)]. The thickness of the film ranged between 0.4 and 1.2 mm. There was no real rain rate that could be associated with the film thickness realized. However, these results are still useful, since they can provide an idea of the effect that the water film has on the radiation pattern.

The magnitude of the measured radiation patterns in each of the scenarios described earlier is compared in Fig. 12 and
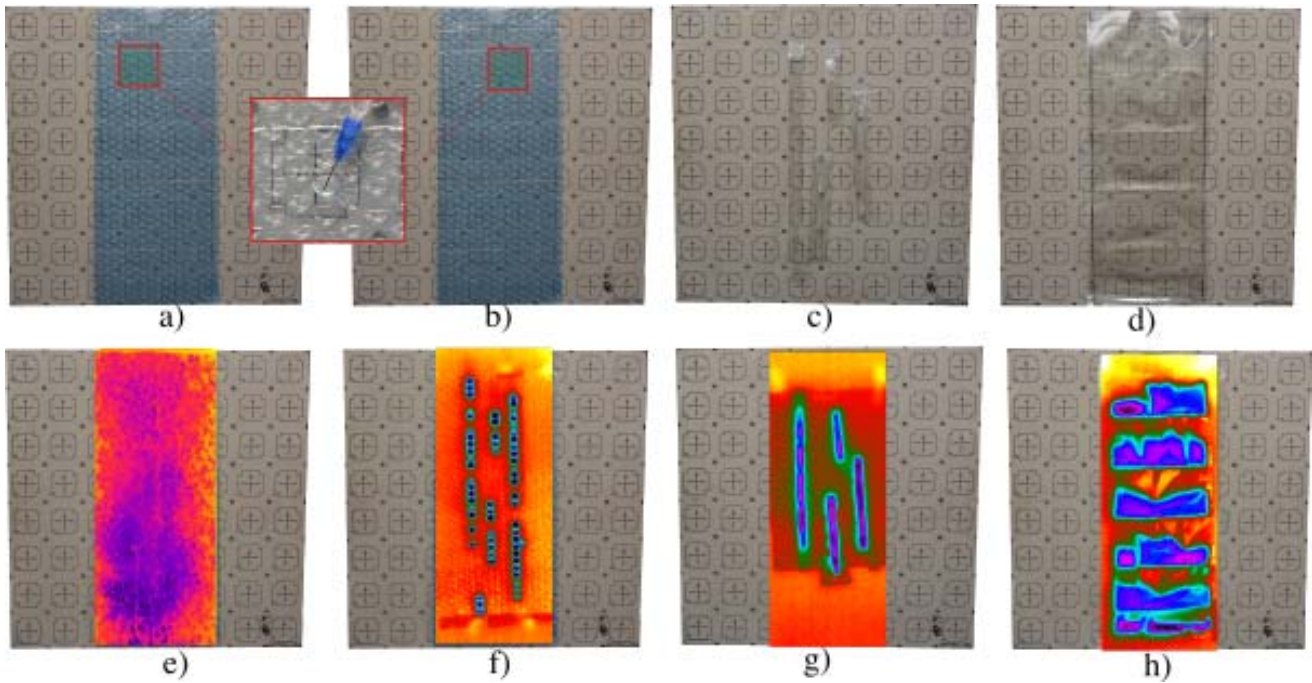
Fig. 11. Photographs of the water placement on the 8×2 array antenna. (a)–(d) Photographs taken with an ordinary camera. (e)–(h) Corresponding photographs taken with the infrared camera. (a) and (e) Droplets. (b) and (f) Vertically aligned droplets. (c) and (g) Rivulets. (d) and (h) Partial water film. Shown in a closeup, the procedure of filling the bubble with water. The temperature range in the photographs is 18°–24 °C, with water being approximately at 19 °C.
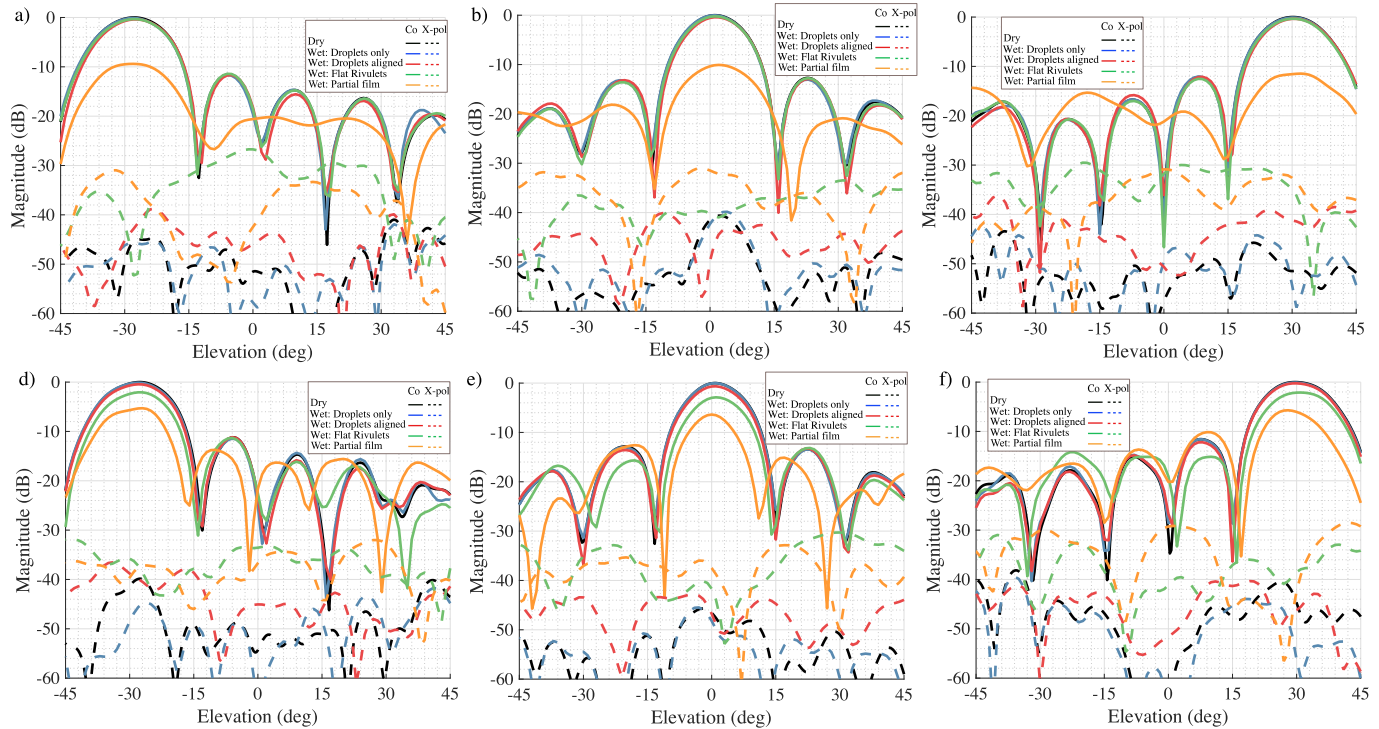
Fig. 12. Effect of water on the magnitude of the 8 × 2 active array antenna LRU far-field radiation pattern. Results were based on near-field measurements under various conditions of the radome. (a)–(c) H-polarization. (d)–(f) V-polarization. (a) and (d) Beam steered at −30°. (b) and (e) Beam at the broadside. (c) and (f) Beam steered at 30°.

summarized in Table II. The attenuation is shown in terms of peak amplitude difference between each of the cases examined. The plots presenting the H-polarization [Fig. 12(a)–(c)] show that the copolarization component is not affected by droplet and rivulet formation. Also, the SLL does not show an appreciable change from the dry case. A strong attenuation is noticeable instead for the water film formation, when the main beam is decreased by 10 dB, the SLL is raised, and
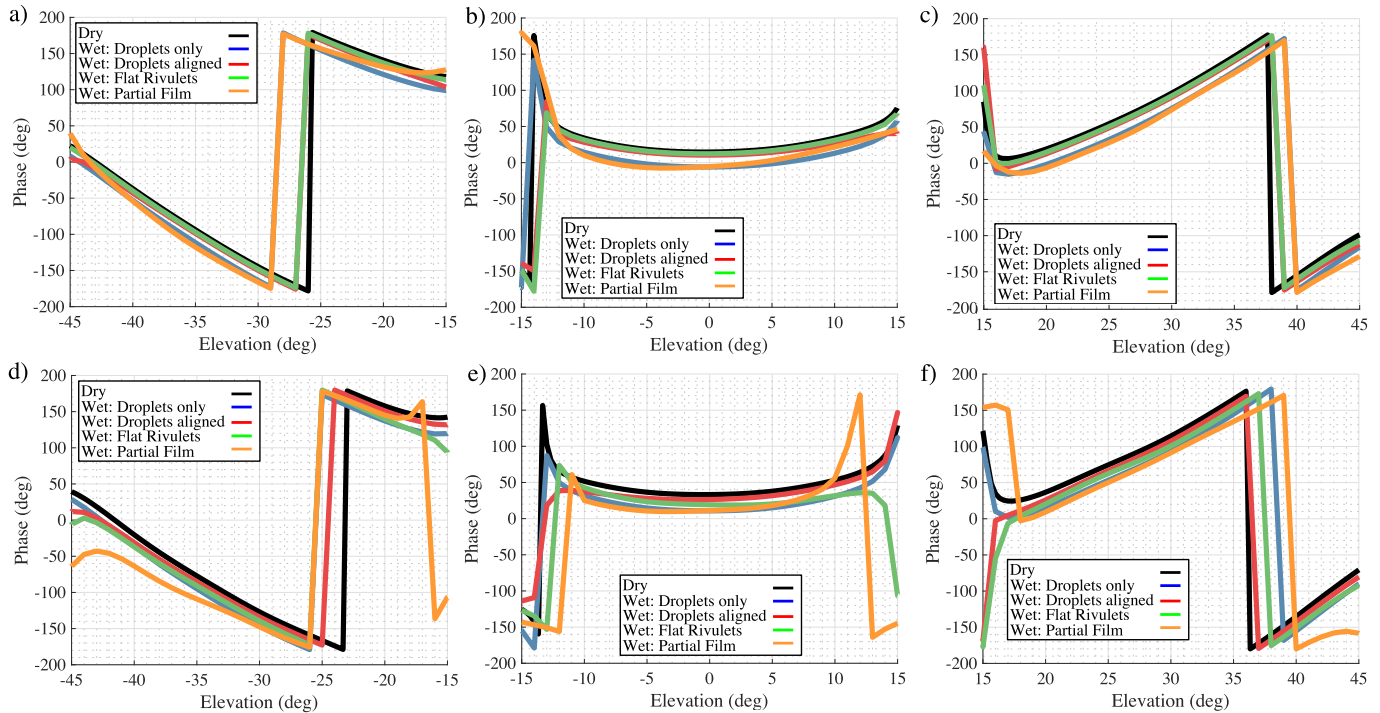
Fig. 13. Effect of water on the phase of the 8×2 active array antenna LRU far-field radiation pattern. Results were based on near-field measurements under various conditions of the radome. (a)–(c) H-polarization. (d)–(f) V-polarization. (a) and (d) Beam steered at $-30°$. (b) and (e) Beam at the broadside. (c) and (f) Beam steered at $30°$.

TABLE II

ATTENUATION (DECIBEL) PRODUCED BY VARIOUS WATER FORMATIONS LOCATED IN THE NEAR-FIELD REGION OF THE ANTENNA. RESULTS BASED ON NEAR-FIELD MEASUREMENTS OF THE 8×2 ACTIVE ARRAY ANTENNA

Water	$\theta_s = -30°$		$\theta_s = 0°$		$\theta_s = 30°$	
	H pol.	V pol.	H pol.	V pol.	H pol.	V pol.
Droplets	0.1	0.1	0.01	0.01	0.09	0.09
Alig. drop.	0.4	0.45	0.41	0.65	0.36	0.25
Rivulets	0.32	2.1	0.23	2.8	0.33	2.1
Part. film	10	5.2	10	6.3	11.5	6

the nulls of the radiation pattern disappeared. The biggest change in the cross-polarization component was obtained for the flat rivulet (green curve) case, when the beam was steered [Fig. 12(a)–(c)]. The partial film formation generated the highest level of cross polarization when the beam was at broadside. The sparse droplet [Fig. 11(e)] and vertically aligned droplet [Fig. 11(f)] cases presented similar magnitudes of cross-polarization levels, regardless of the steering angle. When the signal was vertically polarized, the four cases representing a wet radome presented different responses. Although the water film formation again produced the highest transmission loss of the copolarization component, only an attenuation of 5 dB was noticed. However, for the V-polarization, the nulls of the radiation pattern were still visible and the SLL was less increased with respect to the H-polarization. As expected, because of its vertical geometry, the flat rivulet [Fig. 11(g)] introduced a higher level of attenuation (2 dB) than the H-polarization. The flat rivulets generated a 3 dB attenuation when the

beam was at broadside. Vertically aligned droplets (red curve) generated higher attenuation when the signal was vertically polarized than they did in the H-polarization, although the difference between the two was not large. The level of the cross polarization for the vertically aligned droplet and sparse droplet scenarios was comparable. The flat rivulet and film cases generated almost the same level of cross polarization.

Results for the phase are shown in Fig. 13. The largest phase shift with respect to the dry scenario occurred for the water film case. For a laminar flow, the phase shift was pretty constant at each steering angle considered. It ranged from a minimum of $20.16°$ for the H-polarization with the beam at the broadside to a maximum of $23.14°$ for the V-polarization at a $30°$ steering angle.

C. Summary

A summary of the results obtained in this research and a comparison with the available literature are presented in Table III. This table also lists simulations for additional scenarios that were not plotted for the sake of brevity. Performing numerical simulations for film formation at rain rates of 10–100 mm h^{-1}, with the radome tilted at $\theta_i = 75°$, attenuations between 0.2 and 0.37 dB were obtained. These values fall in the range obtained by Merceret and Ward [26] that computed attenuations from 0.015 to 2.8 dB for rain rates from 1 to 200 mm h^{-1}. An attenuation of 3 dB was obtained in this paper when the radome was characterized in the far field using a single probe. The discrepancy between the numerical and experimental results for film formation is due to the employment of a flat radome for theoretical

TABLE III

Comparison Between the Transmission Losses (*TL*) Obtained in This Research With the Ones Found in the Literature. In the "Approach" Field, for Experimental Scenarios: FF = Far Field and NF = Near Field. Data for NF Experiments Are Reported for $\theta_s = 0°$ for the Polarization That Exhibits the Highest Attenuation. Note: the Two-Way *TL* Found in [26] Is Here Scaled to One-Way *TL* for Consistency

Reference	Approach	R (mm h^{-1})	Water formation	θ_i (°)	TL (dB)
Wilson [23]	Experimental	≤ 90	N/A	N/A	≤ 1
Effenberg [24], Joy [25]	Experimental	15	droplets	60	0.5
		10 - 50	film	60	1.5 - 3
Merceret [26]	Empirical	1 - 200	droplets	N/A	0.005 - 0.98
			film	N/A	0.015 - 2.8
Present study	Numerical	10 - 100	film	90	0.11 - 0.17
				75	0.2 - 0.37
				60	0.23 - 0.5
		10 (T = 9 min)	droplets	75	0.065
		100 (T = 9 min)		75	0.067
	Experimental (FF)	102	film	90	3
	Experimental (NF)	8.9	droplets	0	0.05
		N/A	rivulets	90	2.8
		> 80	film	90	11.5

analysis and a spherical radome panel for the tests. When the geometry is spherical, water accumulates differently [3] than when it is flat (2). A proper comparison with the results available in the literature is hard to perform, because some information about the experiments is not available, such as the direction of water spraying on the radome, which can affect the amount of water collected by the radome area [(2) and (3)]. Experiments performed by Effenberg *et al.* [24] and Joy and Wilson [25] for film formation found transmission losses between 1.5 and 3 dB occurred for rain rates from 10 to 50 mm h^{-1}, which closely approach the experimental results obtained here. When droplet formation was considered, Merceret and Ward [26] found transmission losses from a minimum of 0.005 dB to a maximum of 0.98 dB, for rain rates from 1 to 200 mm h^{-1}. Similarly, in this paper, an attenuation of 0.065 dB was calculated at the rain rate of 10 mm h^{-1} over 9 min of observation time. This result for droplet formation was confirmed by a subsequent experiment in the near field. There is not much difference in attenuation between 10 and 100 mm h^{-1} for T = 9 min because after such a long observation time, the radome becomes saturated in terms of droplet accumulation. For droplet formation, a proper comparison between different studies is hard to perform, because the observation time can be a critical factor at the moment of the attenuation measurement. In addition, when the surface of the radome is hydrophobic, droplets and rivulets present simultaneously (Fig. 1). Therefore, it is hard to distinguish the contribution of rivulets from that of droplets.

V. Conclusion

This paper discussed the impact of a wet radome on the performance of an active phased-array antenna for weather observations. Analytical formulations and numerical analysis were performed to provide preliminary values on the levels of attenuation introduced by the radome under droplet and film formations. First, experiments on a radome of an operative weather radar were performed to evaluate the effect of water in the far field. Subsequent experiments in near field were executed to measure the degradation introduced by water into the far-field radiation pattern. For the experiments performed in the near-field chamber, an active array antenna of 8 × 2 elements operating at the *S*-band was used. The current results show a good agreement with available literature. Results from both numerical analysis and experiments show that higher attenuation occurs when water distributes as a film. Droplet formation does not critically compromise the operation of a radar antenna until rivulets are generated. However, when rivulets form, this paper demonstrated how their presence critically impacts V-polarized signals. Although rivulets mostly influence the signal when it is vertically polarized, a rise in the cross-polarization level also occurs when the signal is horizontally polarized. In conclusion, results of this paper highlighted that the *S*-band radars are critically affected by the presence of water, showing that significant attenuation occurs both when the radome presents hydrophobic (droplets and rivulets) and hydrophilic (film) properties.

References

[1] J. D. Walton, Ed., *Radome Engineering Handbook: Design and Principles*. New York, NY, USA: Marcel Dekker, 1970.

[2] J. A. Vitale, *Microwave Scanning Antennas*, vol. 1. Newport Beach, CA, USA: Peninsula Publishing, 1985, ch. 5.

[3] D. Gibble, "Effect of rain on transmission performance of a satellite communication system," in *Proc. IEEE Int. Conv. Rec. VI*, 1964, p. 52.

[4] B. Blevis, "Losses due to rain on radomes and antenna reflecting surfaces," *IEEE Trans. Antennas Propag.*, vol. 13, no. 1, pp. 175–176, Jan. 1965.

[5] A. Cohen and A. Smolski, "The effect of rain on satellite communications earth terminal rigid radomes," *Microw. J.*, vol. 9, pp. 111–121, 1966.

[6] I. Anderson, "Measurements of 20-GHz transmission through a radome in rain," *IEEE Trans. Antennas Propag.*, vol. 23, no. 5, pp. 619–622, Sep. 1975.

[7] C. E. Hendrix, J. E. McNally, and R. A. Monzingo, "Depolarization and attenuation effects of radomes at 20 GHz," *IEEE Trans. Antennas Propag.*, vol. 37, no. 3, pp. 320–328, Mar. 1989.

[8] K.-C. Chang, "System performance in rain in a radome-enclosed environment," in *Proc. IEEE Military Commun. Conf. (MILCOM)*, vol. 1, Oct. 1985, pp. 293–299.

[9] A. J. Fenn, "Measurements of wet radome transmission loss and depolarization effects in simulated rain at 20 GHz," in *Proc. 10th Int. Conf. Antennas Propag.*, vol. 1, Apr. 1997, pp. 474–477.

[10] R. K. Crane, "Analysis of the effects of water on the ACTS propagation terminal antenna," *IEEE Trans. Antennas Propag.*, vol. 50, no. 7, pp. 954–965, Jul. 2002.

[11] D. S. Zrnić and R. J. Doviak, "System requirements for phased array weather radar," NOAA/NSSL, Norman, OK, USA, NOAA/NSSL Rep., 2005.

[12] Y. Wang and V. Chandrasekar, "Polarization isolation requirements for linear dual-polarization weather radar in simultaneous transmission mode of operation," *IEEE Trans. Geosci. Remote Sens.*, vol. 44, no. 8, pp. 2019–2028, Aug. 2006.

[13] S. J. Frasier *et al.*, "In-place estimation of wet radome attenuation at X band," *J. Atmos. Ocean. Technol.*, vol. 30, no. 5, pp. 917–928, 2013.

[14] E. Gorgucci, R. Bechini, L. Baldini, R. Cremonini, and V. Chandrasekar, "The influence of antenna radome on weather radar calibration and its real-time assessment," *J. Atmos. Ocean. Technol.*, vol. 30, no. 4, pp. 676–689, 2012.

[15] M. Schneebeli *et al.*, "Polarimetric X-band weather radar measurements in the tropics: Radome and rain attenuation correction," *Atmos. Meas. Techn.*, vol. 5, no. 9, pp. 2183–2199, 2012.

[16] J. L. Salazar-Cerreño *et al.*, "A drop size distribution (DSD)-based model for evaluating the performance of wet radomes for dual-polarized radars," *J. Atmos. Ocean. Technol.*, vol. 31, no. 11, pp. 2409–2430, 2014.

[17] J. Díaz, J. L. Salazar, A. Mancini, and J. G. Colom, "Radome design and experimental characterization of scattering and propagation properties for atmospheric radar applications," in *Proc. Amer. Meteorol. Soc.*, 2014, pp. 819–823.

[18] A. Mancini, J. L. Salazar, R. M. Lebrón, and B. L. Cheong, "A novel instrument for real-time measurement of attenuation of weather radar radome including its outer surface. Part I: The concept," *J. Atmos. Ocean. Technol.*, vol. 35, no. 5, pp. 953–973, 2018.

[19] A. Mancini, J. L. Salazar, R. M. Lebrón, and B. L. Cheong, "A novel instrument for real-time measurement of attenuation of weather radar radome including its outer surface. Part II: Applications," *J. Atmos. Ocean. Technol.*, vol. 35, no. 5, pp. 975–991, 2018.

[20] A. Mancini, J. L. Salazar, R. M. Lebrón, and B. L. Cheong, "A novel technique to characterize the effect of rain over a radome for radar applications," in *Proc. IEEE Radar Conf. (RadarConf)*, May 2017, pp. 470–475.

[21] M. Frech, B. Lange, T. Mammen, J. Seltmann, C. Morehead, and J. Rowan, "Influence of a radome on antenna performance," *J. Atmos. Ocean. Technol.*, vol. 30, no. 2, pp. 313–324, 2012.

[22] M. Kurri and A. Huuskonen, "Measurements of the transmission loss of a radome at different rain intensities," *J. Atmos. Ocean. Technol.*, vol. 25, no. 9, pp. 1590–1599, Sep. 2008.

[23] J. W. Wilson, "Observations of radome transmission losses at 5 cm wavelengths," in *Proc. 18th Conf. Radar Meteorol. Amer. Meteorol. Soc.*, 1978, pp. 288–291.

[24] J. A. Effenberger, R. R. Strickland, and E. B. Joy, "The effects of rain on a Radome's performance," *Microw. J.*, vol. 29, no. 9, pp. 261–264, May 1986.

[25] E. B. Joy and R. E. Wilson, "The electromagnetic effects of water on the surface of a radome," in *Proc. 18th Symp. Electromagn. Windows*, 1986, pp. 27–32A.

[26] F. J. Merceret and J. G. Ward, "Attenuation of weather radar signals due to wetting of the radome by rainwater or incomplete filling of the beam volume," NASA, Cocoa Beach, FL, USA, Tech. Rep. NASA/TM-2002-211171, 2002.

[27] A. Ryzhkov and D. S. Zrnić, "Precipitation and attenuation measurements at a 10-cm wavelength," *J. Appl. Meteorol.*, vol. 34, no. 10, pp. 2121–2134, 1995.

[28] J. D. Díaz *et al.*, "A dual-polarized cross-stacked patch antenna with wide-angle and low cross-polarization for fully digital multifunction phased array radars," in *Proc. IEEE Int. Symp. Phased Array Syst. Technol. (PAST)*, Oct. 2016, pp. 1–4.

[29] R. H. Perry, *Perry's Chemical Engineers' Handbook*. New York, NY, USA: McGraw-Hill, 1997.

[30] G. Zhang, J. Vivekanandan, and E. Brandes, "A method for estimating rain rate and drop size distribution from polarimetric radar measurements," *IEEE Trans. Geosci. Remote Sens.*, vol. 39, no. 4, pp. 830–841, Apr. 2001.

[31] D. Atlas and C. W. Ulbrich, "Path- and area-integrated rainfall measurement by microwave attenuation in the 1–3 cm band," *J. Appl. Meteorol.*, vol. 16, no. 12, pp. 1322–1331, Sep. 2018.

[32] R. J. Doviak and D. S. Zrnić, *Doppler Radar and Weather Observations*. New York, NY, USA: Academic, 1993.

[33] M. Steiner and J. A. Smith, "Reflectivity, rain rate, and kinetic energy flux relationships based on raindrop spectra," *J. Appl. Meteorol.*, vol. 39, no. 11, pp. 1923–1940, 2000.

[34] M. A. Nilsson and J. P. Rothstein, "Using sharp transitions in contact angle hysteresis to move, deflect, and sort droplets on a superhydrophobic surface," *Phys. Fluids*, vol. 24, no. 6, p. 062001, 2012.

[35] A. H. Sihvola, "Mixing rules with complex dielectric coefficients," *Subsurf. Sens. Technol. Appl.*, vol. 1, no. 4, pp. 393–415, Oct. 2000.

Alessio Mancini (S'10) received the B.S. and M.S. degrees in electrical engineering from the University of Bologna, Bologna, Italy, in 2007 and 2011, respectively. He is currently pursuing the Ph.D. degree with The University of Oklahoma, Norman, OK, USA.

He is currently a Graduate Research Assistant with the Phased Array Antenna Research and Development Group, Advanced Radar Research Center, The University of Oklahoma, under the supervision of Dr. J. L. Salazar. His current research interests include antenna design, electromagnetic modeling, radome design, characterization, and calibration.

Rodrigo M. Lebrón (S'16) received the B.S. degree in mechatronics from the Universidad Nacional de Asunción, San Lorenzo, Paraguay, in 2012, and the M.S. degree in mechanical engineering from the Universidade Federal do Rio Grande do Sul, Porto Alegre, Brazil, in 2015. He is currently pursuing the Ph.D. degree in electrical and computer engineering with The University of Oklahoma, Norman, OK, USA.

He is currently a Graduate Research Assistant with the Phased Array Antenna Research and Development Group, Advanced Radar Research Center, The University of Oklahoma, under the supervision of Dr. J. L. Salazar. His current research interests include phased-array antenna design, thermal analysis, and active array characterization and calibration.

Jorge L. Salazar (S'00–M'12–SM'14) received the B.S. degree in electrical engineering from University Antenor Orrego, Trujillo, Peru, in 1994, the M.S. degree in electrical engineering from the University of Puerto Rico at Mayagüez, Mayagüez, Puerto Rico, in 2003, and the Ph.D. degree from the University of Massachusetts Amherst, Amherst, MA, USA, in 2012.

In 2012, he joined the Department of Electrical and Computer Engineering, University of Puerto Rico at Mayagüez, as an Adjunct Professor. In 2012, he also joined the Advanced Radar Research Center, The University of Oklahoma, Norman, OK, USA, as a Research Scientist. In 2015, he joined the School of Electrical and Computer Engineering, The University of Oklahoma, as an Assistant Professor. His current research interests include active phased-array antenna design and calibration for the next radar generation.

Dr. Salazar was a recipient of the National Center for Atmospheric Research Advanced Study Program Post-Doctoral Fellowship in 2012.